Whole-brain functional imaging at cellular resolution using light-sheet microscopy

Misha B Ahrens & Philipp J Keller

Brain function relies on communication between large populations of neurons across multiple brain areas, a full understanding of which would require knowledge of the time-varying activity of all neurons in the central nervous system. Here we use light-sheet microscopy to record activity, reported through the genetically encoded calcium indicator GCaMP5G, from the entire volume of the brain of the larval zebrafish *in vivo* at 0.8 Hz, capturing more than 80% of all neurons at single-cell resolution. Demonstrating how this technique can be used to reveal functionally defined circuits across the brain, we identify two populations of neurons with correlated activity patterns. One circuit consists of hindbrain neurons functionally coupled to spinal cord neuropil. The other consists of an anatomically symmetric population in the anterior hindbrain, with activity in the left and right halves oscillating in antiphase, on a timescale of 20 s, and coupled to equally slow oscillations in the inferior olive.

Although single-neuron recordings have revealed much about neural processing, recordings from larger populations can lead to fundamentally different insights. These include understanding how neuronal ensembles code for sensory input[1–5], implement sensorimotor transformations[6], drive motor output[7] or partake in spontaneous activity[8].

Though optical[9–14] and electrophysiological[7,15] techniques exist for recording from many neurons, the number of simultaneously recorded neurons, as a fraction of the number of neurons in the brain, is typically still tiny. This limitation arises from constraints on the number of neurons that can be imaged at the same time and the total brain size of the animal under study. Thus, interactions between neurons in different brain areas are easily missed, and functionally related ensembles of neurons are undetectable if their activity is not tightly locked to a temporal reference such as sensory input or features of behavior. Not only would the ability to simultaneously record from all neurons in a brain make it possible to address questions that cannot be answered with conventional techniques, it also would vastly speed up the throughput of experiments that can be performed with existing approaches.

Here we use high-speed light-sheet microscopy to image almost all neurons in the intact larval zebrafish brain at single-cell resolution, capturing activity in the entire brain once every 1.3 s. Activity was reported by the genetically encoded calcium indicator GCaMP5G[16] expressed under the control of the pan-neuronal *elavl3* promoter[17]. To achieve the volumetric imaging speed required for fast three-dimensional recordings of the entire larval zebrafish brain, which is composed of ~100,000 neurons[18], we extended the capabilities of the SiMView light-sheet microscopy framework[19]. We increased the sustained volumetric imaging rate approximately tenfold over previously reported performance in state-of-the-art light-sheet microscopy[12,19] and achieved cellular resolution for more than 80% of all neurons. This allows, for the first time, almost exhaustive imaging of single-neuron activity in the brain of a vertebrate.

To examine the functional and anatomical structure of activity patterns across the brain, we developed a computational method for identifying correlated population activity with a given spectrum of temporal dynamics. This analysis led to the identification of two functional networks that span large areas of the hindbrain and may be involved in locomotion.

RESULTS

Whole-brain functional imaging at single-neuron resolution

We used laser-scanning light-sheet microscopy[20] to image the entire brain of the larval zebrafish with single-cell resolution for more than 80% of all neurons (**Fig. 1a**). To achieve the imaging speed required for exhaustive functional imaging with calcium indicators, whose dynamics are on the timescale of a second, we extended the capabilities of the SiMView implementation of light-sheet microscopy[19]. We redesigned the volumetric imaging strategy, eliminated electronic overhead and integrated new detectors, thereby enhancing the sustained volumetric imaging rate of the SiMView platform approximately tenfold (Online Methods). This enables high-speed live imaging of the entire larval zebrafish brain, covering a volume of $800 \times 600 \times 200\ \mu m^3$ in ~1.3 s (**Fig. 1b** and **Supplementary Video 1**).

We recorded continuously for approximately 1 h without external stimulation, using one-photon excitation with either one or two light sheets entering the brain from the side. We used the *albino* (*slc45a2*) mutant, whose lack of pigmentation on the outside of the eye allowed us to scan through the eye and excite tissue also between the eyes.

To achieve full physical coverage of the brain at cellular resolution, we recorded the volume plane by plane in steps of 5 μm with

Howard Hughes Medical Institute, Janelia Farm Research Campus, Ashburn, Virginia, USA. Correspondence should be addressed to M.B.A. (ahrensm@janelia.hhmi.org) or P.J.K. (kellerp@janelia.hhmi.org).

RECEIVED 9 JANUARY; ACCEPTED 12 MARCH; PUBLISHED ONLINE 18 MARCH 2013; DOI:10.1038/NMETH.2434

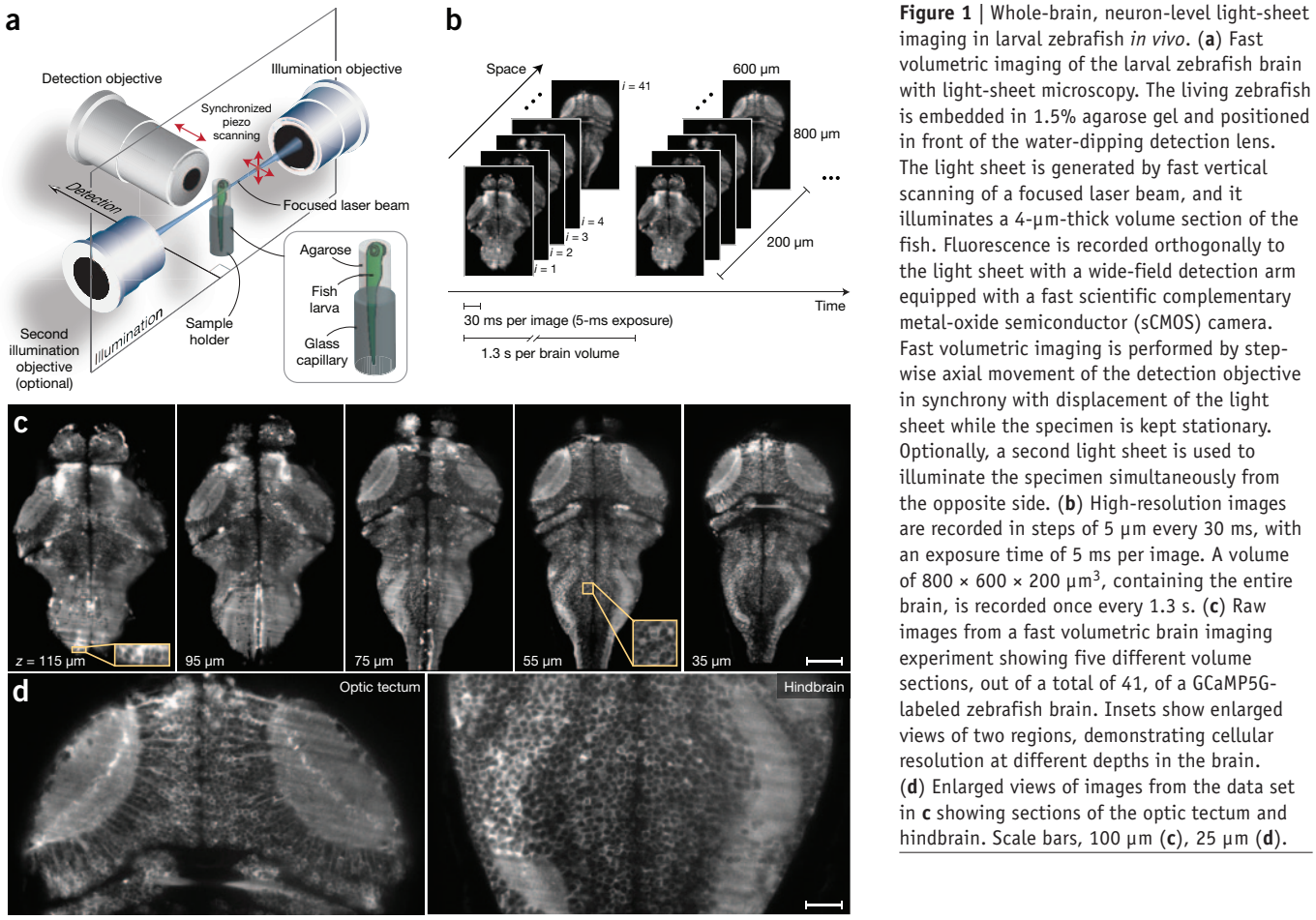

Figure 1 | Whole-brain, neuron-level light-sheet imaging in larval zebrafish *in vivo*. (**a**) Fast volumetric imaging of the larval zebrafish brain with light-sheet microscopy. The living zebrafish is embedded in 1.5% agarose gel and positioned in front of the water-dipping detection lens. The light sheet is generated by fast vertical scanning of a focused laser beam, and it illuminates a 4-µm-thick volume section of the fish. Fluorescence is recorded orthogonally to the light sheet with a wide-field detection arm equipped with a fast scientific complementary metal-oxide semiconductor (sCMOS) camera. Fast volumetric imaging is performed by stepwise axial movement of the detection objective in synchrony with displacement of the light sheet while the specimen is kept stationary. Optionally, a second light sheet is used to illuminate the specimen simultaneously from the opposite side. (**b**) High-resolution images are recorded in steps of 5 µm every 30 ms, with an exposure time of 5 ms per image. A volume of 800 × 600 × 200 µm^3, containing the entire brain, is recorded once every 1.3 s. (**c**) Raw images from a fast volumetric brain imaging experiment showing five different volume sections, out of a total of 41, of a GCaMP5G-labeled zebrafish brain. Insets show enlarged views of two regions, demonstrating cellular resolution at different depths in the brain. (**d**) Enlarged views of images from the data set in **c** showing sections of the optic tectum and hindbrain. Scale bars, 100 µm (**c**), 25 µm (**d**).

a light sheet 4.25 ± 0.80 µm thick (full width at half maximum, mean ± s.d. across brain volume, $n = 81$), which is slightly more than half the average diameter of cell bodies (6.62 ± 0.14 µm, mean ± s.e.m., $n = 298$). The effective lateral resolution of 0.65 µm of our optical configuration[19] is about one-tenth of the average size of cell bodies. Owing to the high transparency of larval *albino* zebrafish, neighboring neurons were thus generally easily separable within one optical section, both in deep and in superficial layers of the brain (**Fig. 1c**,**d** and **Supplementary Videos 1** and **2**). A systematic analysis of resolution and image contrast for the entire brain anatomy showed that approximately 86.9% of all neurons were captured with subcellular lateral resolution (**Supplementary Fig. 1a**). The remaining brain volume was partially shadowed by the eyes (10.8%) or was recorded with lower image contrast because of refraction of the light sheet in the specimen (2.3%) (**Supplementary Fig. 1b**–**g**).

By comparing the functional light-sheet data to a detailed gold-standard two-photon recording and segmenting regions captured with subcellular lateral resolution, we estimated that at least 92.0% of the cell bodies were resolved at the single-cell level in the light-sheet data (Online Methods). The overall fraction of brain volume covered with single-cell resolution is thus estimated to be at least 80% (92.0% × 86.9%).

This is a conservative estimate because we used only anatomy data to separate neighboring neurons. Generally, only a small fraction of neurons exhibit strong activity at the same time and only a subset of these neurons are direct neighbors along the detection axis. Thus, to complement the analysis of anatomy-based single-cell resolution, we also inspected slices and top and side projections of changes in fluorescence intensity ($\Delta F/F$) (**Fig. 2** and **Supplementary Videos 3**–**6**) in multiple layers of the hindbrain at time points when large groups of neurons showed raised activity levels. In both projection views, single-neuron shapes were apparent (**Fig. 2b**). Neurons identified from the top projection, where they were visible in high detail because of the subcellular lateral resolution, could also be unambiguously identified in the side projection. Even in those rare cases in which directly neighboring neurons were active at the same time and located at the same lateral position (that is, displaced along only the detection axis), neighbors could usually be separated based solely on their $\Delta F/F$ signals (**Fig. 2b**).

We determined an average signal-to-noise ratio of 180 ± 11 (mean ± s.e.m., $n = 31$; not considering the signal-to-noise ratio of the calcium indicator itself, see Online Methods) for neurons in different regions of the light sheet–based whole-brain recording. Owing to this high ratio and the short volumetric imaging interval, which was comparable to the time course of GCaMP5G at room temperature[16], the occurrence of action potentials within the recording interval was detectable in most cases (**Supplementary Fig. 2**).

Characterization of correlations across brain areas

A key advantage of whole-brain light-sheet imaging is the capability to simultaneously interrogate activity patterns in disparate brain

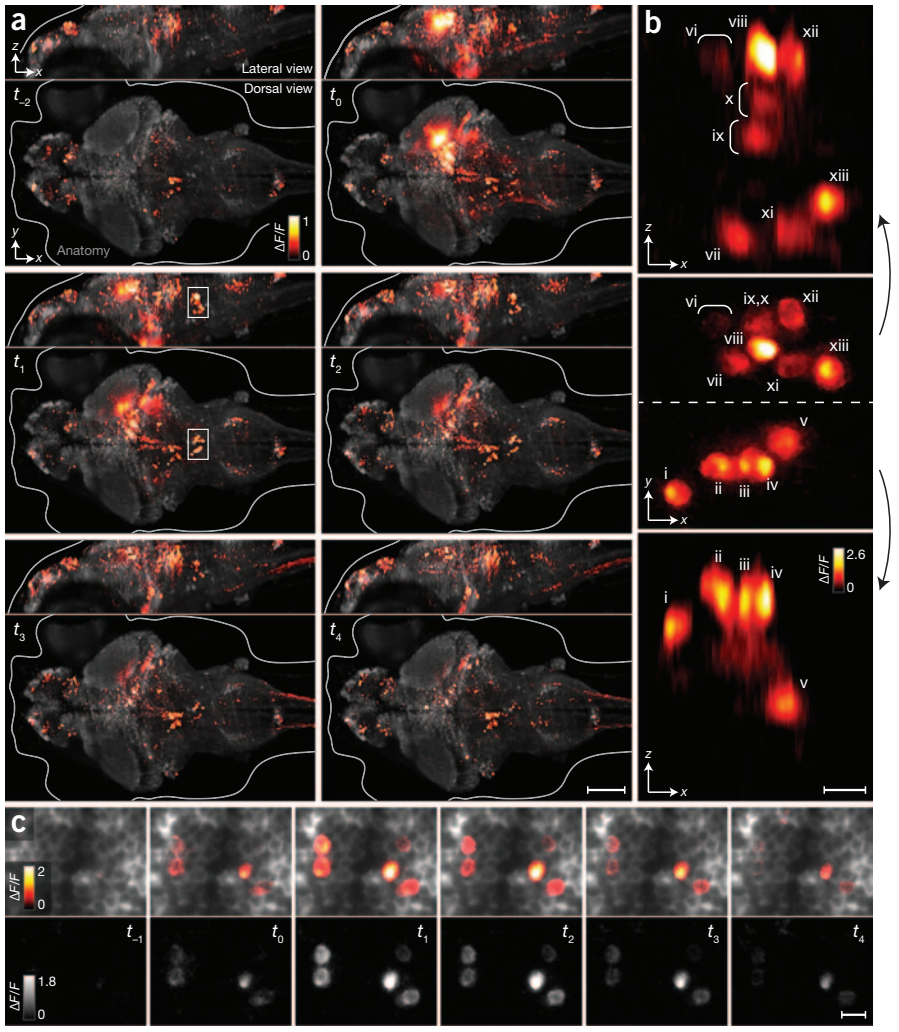

Figure 2 | Whole-brain imaging of neuronal activity with cellular resolution. (**a**) Dorsal and lateral projections of whole-brain, neuron-level functional activity, reported by the genetically encoded calcium indicator GCaMP5G in an *elavl3:GCaMP5G* fish via changes in fluorescence intensity ($\Delta F/F$), superimposed on the reference anatomy. Panels represent whole-brain volumes recorded in intervals of 1.39 s. Near-simultaneous activation of a large population of neurons occurs at the second frame (t_0) and spans areas in the midbrain and hindbrain. (**b**) Enlarged view of the region outlined in dorsal (*xy*) and lateral (*xz*) projections shown in panel t_1 in **a**, demonstrating cellular resolution in the whole-brain recordings. For visualization purposes, bicubic interpolation was used to generate isotropic voxel sizes. In the dorsal projection, 13 neuron identities are indicated (i–xiii). Separate lateral projections are shown for the two halves of this volume. Every neuron visible in the top projection can also be identified in the side projection. (**c**) Activity at the single-neuron level in a single slice from the volume visualized in **b**. Activity is shown superimposed on the anatomy (top) as well as separate from the anatomy (bottom). Slices represent activity recorded at consecutive intervals of 1.39 s. Scale bars, 100 µm (**a**), 10 µm (**b**,**c**).

regions and to relate these to one another. As a first high-level analysis, we segmented the brain into 11 regions (**Fig. 3a**) and derived average fluorescence time series across each of these regions (**Fig. 3b**). Average activity in most brain areas was characterized by large, temporally sparse increases in fluorescence. In many cases, these discharges occurred synchronously across the hindbrain and the midbrain (**Fig. 3b**). Areas of the forebrain—the habenula and the pallium—formed an exception, with average activity characterized by ongoing, slow fluctuations (**Fig. 3b**), which appeared to be independent of the discharges in the mid- and hindbrain. We investigated the correlational structure of activity across these brain regions by calculating the correlation coefficients between the fluorescence traces. Areas of the midbrain showed strong correlations (**Fig. 3c**,**d**), as did areas of the hindbrain. Mid- and hindbrain activity was also correlated, although to a lesser degree. The latter result is consistent with previous observations of simultaneous activity in tectal neurons and tail flicks of head-embedded larvae[21] and of the involvement of hindbrain neurons in swimming[22,23], which together suggest the presence of coincident activation in the tectum and the hindbrain.

All forebrain areas showed strong correlations to each other. However, the average activity of forebrain areas appeared to be relatively uncorrelated to activity in the mid- and hindbrain areas (**Fig. 3d**,**e**). This was surprising, given the previous finding of motor-related neurons in the forebrain[9], and motivated our subsequent single-neuron analysis.

Analysis of single-neuron habenula activity

The above brain-area analysis may miss correlations between single neurons. For instance, if hindbrain circuits drive one neuron population in a forebrain area and inhibit another, single-neuron correlations will be averaged out and remain undetected. To examine the apparent independence between the forebrain and the mid- and hindbrain suggested by **Figure 3**, we manually segmented neurons from the entire left habenula. We ordered the fluorescence traces from ~300 habenula neurons according to their correlation to average hindbrain activity (**Fig. 4a**). Indeed, some neuronal subpopulations were coactivated with peaks in hindbrain activity, whereas others were suppressed. This is consistent with the presence of forebrain activity correlated and anticorrelated to motor output reported previously[9]. A shuffle test confirmed that these correlations did not arise by chance (Online Methods).

As already seen in the average activity of forebrain areas (**Fig. 3**), activity in many of these habenula neurons appeared to exhibit slower fluctuations and longer timescales than activity elsewhere in the brain (for example, neurons in **Fig. 4b**). To examine the temporal structure of neural activity on the spatial scale of neurons, we divided the entire brain into neuron-sized supervoxels ($5 \times 5 \times 5\ \mu m^3$), extracted $\Delta F/F$ averaged over all voxels in each supervoxel and applied Fourier analysis to these signals to construct the power spectrum associated with each supervoxel. To compare brain areas, we averaged the power spectra over all supervoxels in the forebrain and over the mid- and hindbrain. This revealed higher power in the forebrain in

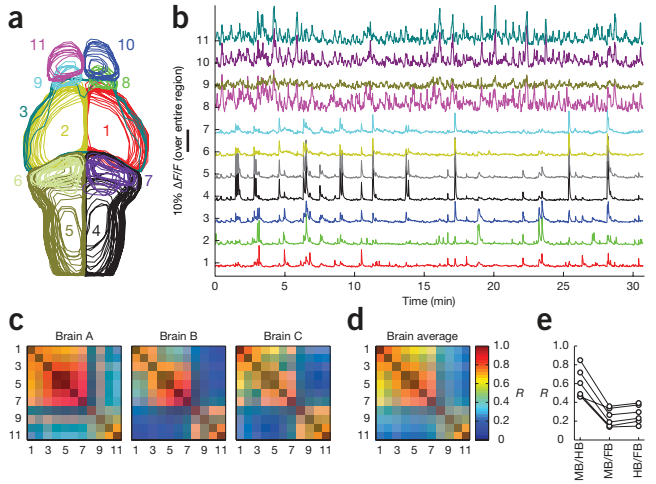

Figure 3 | Correlations and activity patterns across brain regions. (**a**) Manual segmentation of brain regions. 1,2: right and left midbrain; 3: ventral midbrain; 4,5: right and left hindbrain; 6,7: cerebellum; 8,9: habenula; 10,11: pallium. (**b**) Fluorescence ($\Delta F/F$) traces in each brain area of **a** in a transgenic fish expressing GCaMP5G in almost all neurons (*elavl3:GCaMP5G*). Hindbrain areas (4–7) are often activated together, and midbrain activation (1–3) sometimes co-occurs with hindbrain activation. Forebrain activity is qualitatively distinct, characterized by ongoing activity, at long timescales (on the order of 10 s). Average forebrain activity is not clearly coactivated with mid- and hindbrain activity. (**c**) Correlation matrices of brain area activity for three fish (Brains A, B and C); numbering as in **a**. Mid- and hindbrain activity are self-correlated and correlated to each other; activity in forebrain areas is self-correlated; and average forebrain activity appears weakly correlated to mid- and hindbrain activity. Note that zero correlation for activity averaged over brain areas does not necessarily imply the absence of correlations on the single-neuron level (see **Fig. 4**) and that correlational structure reflects activity in the particular experimental conditions used to derive these data. (**d**) Average correlation coefficients (R) of six fish. (**e**) Correlations between the entire hindbrain (HB), midbrain (MB) and forebrain (FB) for six fish.

the band between 10 s and several minutes (**Fig. 4c**). Low-frequency ongoing neural activity has been observed in brains of mammals, and its function and mechanism are poorly understood[8,24]. We were intrigued by the slow ongoing processes exhibited by zebrafish forebrain neurons and asked whether, across the entire brain, other neuronal populations exist with similarly long-timescale activity patterns.

Correlational analysis of whole-brain single-cell activity

As a first step in investigating whole-brain circuit function, our next goal was to find, across the entire brain, functionally coupled large populations of neurons with slow, correlated activity (Online Methods and **Supplementary Software**). We developed an analysis method that is based on the idea that if activity of a large population of neurons is highly correlated, it should be possible to recover the subcellular anatomy[25] of the entire population by correlating every voxel in the volumetric recording to the time-varying activity of a single neuron of the population (referred to as the reference trace; Online Methods and **Fig. 5**). Voxels that are part of cell bodies or neurites in the population will have high absolute correlation to the activity of the single neuron; voxels that are not part of the population will have low correlation.

If activity of a single neuron can thus recover such an entire functionally defined circuit, the challenge, then, is to find a neuron that is part of a larger population with highly correlated activity patterns. To this end, our method first identified candidate neurons (more precisely, neuron-sized supervoxels) that appeared to be part of a large, strongly correlated population, using an ordered correlation matrix for supervoxels preselected for long timescales (Online Methods and **Fig. 5**, steps 1–3).

Once such a candidate was found, we correlated its time-varying activity to the entire volumetric data set to extract the morphology of the entire population (Online Methods and **Fig. 5**, steps 4–6). After the anatomy of the functional circuit was thus recovered, we inspected the activity time series of individual neurons of the population to generate an anatomical and functional characterization of the circuit (Online Methods and **Fig. 5**, step 6). In this way we identified two functionally defined circuits that were consistently present across fish.

The hindbrain oscillator

A reference signal (that is, the functional activity of one supervoxel with strong correlations to many other supervoxels) that was con-

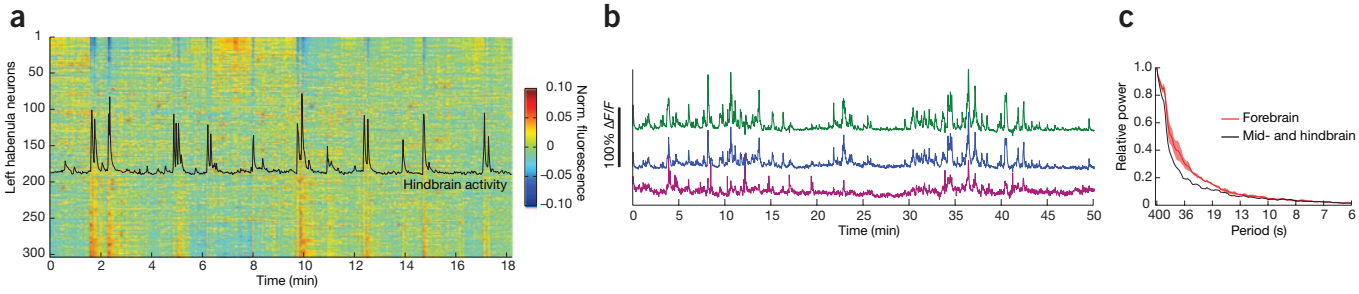

Figure 4 | Single-neuron activity in the left habenula and correlation to hindbrain activity. (**a**) Activity traces of all neurons in a manually segmented habenula. Habenula neuron activity traces are ordered by correlation coefficient to average hindbrain activity (black trace), with negative correlations at the top and positive correlations at the bottom. Populations that are both strongly positively correlated and negatively correlated are present, as are neurons with ongoing, uncorrelated activity. (**b**) Three examples of activity traces of habenula neurons. Single-neuron activity is ongoing, with fluctuations on timescales of ~10–30 s, and can in addition be modulated on timescales of minutes, switching between ongoing activity and apparent quiescence. (**c**) Power spectra of $\Delta F/F$ signals from all supervoxels in the forebrain and all supervoxels in the mid- and hindbrain. Shaded regions show standard error. Data were normalized to the average mid- and hindbrain power spectra, so that the black line does not carry error bars (for a_i and b_i being the forebrain and midbrain/hindbrain power spectra for fish i, respectively, and b_{avg} the average of all b_i, plotted are b_{avg} (black) and $a_i \times b_{avg} / b_i$ (red, mean ± s.d.)). Relative power in the forebrain is enhanced on timescales between 10 s and several minutes.

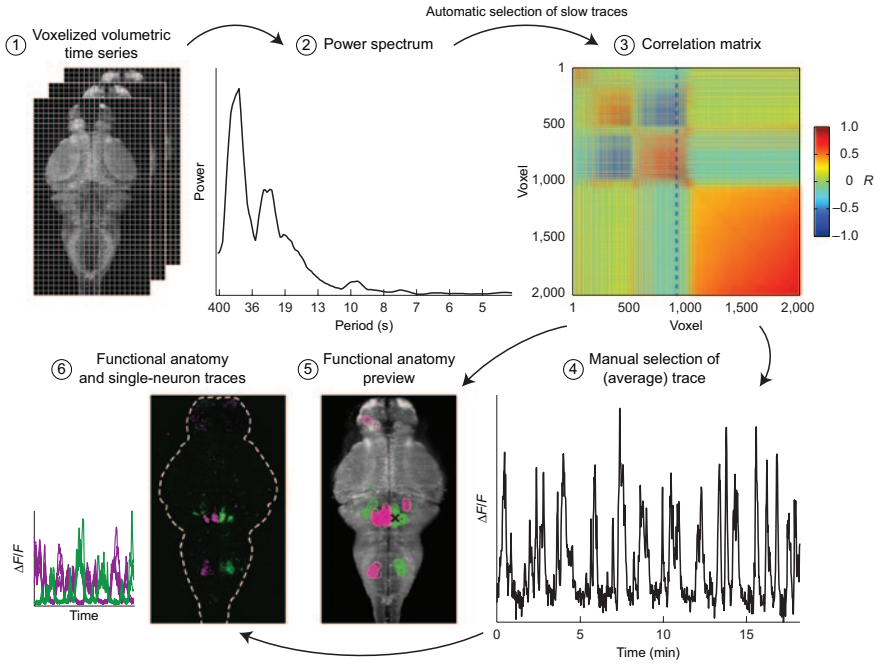

Figure 5 | Semiautomated analysis procedure for volumetric imaging of non–stimulus locked, long-timescale activity. Step 1: schematic for brain partitioning into supervoxels (5 × 5 × 5 μm^3, approximate soma size). Average functional fluorescence ($\Delta F/F$) traces are obtained for each of the approximately 500,000 supervoxels. Step 2: the power spectrum of each functional trace (one example shown) is used for extracting long-timescale signals. Ordering is based on difference in total power in the bands 10–30 s and 2–10 s. The top 2,000 entries are selected for further analysis. Step 3: matrix of correlation coefficients for $\Delta F/F$ of all selected supervoxels. Supervoxels are ordered by the number of correlated supervoxels with correlation >0.5, in some cases forming clusters (the rightmost column contains the largest number of strongly correlated supervoxels). Individual supervoxels are manually selected for further analysis. Step 4: example reference trace manually selected on the basis of the correlation matrix. The trace corresponds to the supervoxel indicated by the dashed line in step 3, the position of which is marked by "X" in step 5. Step 5: top projection of locations of supervoxels with strong positive (>0.5, green) or negative (<–0.5, magenta) correlations to the reference trace (step 4). Anatomical clustering becomes apparent. Step 6: every voxel in the brain is correlated to the reference trace, with correlation coefficients forming a functional anatomical map. The maximum-intensity projection of this correlation map is shown. Green, positive correlations; magenta, negative correlations. Single-neuron shapes become visible and can be segmented to obtain functional traces (left).

sistently found across fish was slowly fluctuating and was approximately oscillatory with a period of 20–30 s (for example, the signal in **Fig. 5**, step 4, or **Fig. 6**). Correlation of this reference signal with the ~20 min of recorded volumes yielded populations of neurons in the anterior hindbrain, behind the cerebellum (**Fig. 6a**,**b** and **Supplementary Video 7**). The populations of neurons to the left and right of the midline were symmetric, with one exhibiting positive correlations to the reference signal and the other exhibiting negative correlations (**Fig. 6a**,**b**). This suggests that the populations oscillate in antiphase, which we later confirmed by functional analysis of single neurons. For brevity, this structure is henceforth referred to as the hindbrain oscillator.

A second structure with neuronal activity correlated to the reference signal was located posterior to the hindbrain oscillator. On the basis of anatomical location[9] and comparison to a *vglut2a:DsRed* line[23], this structure is likely to be part of the lateral inferior olive (**Fig. 6a**,**b**). The left and right inferior olive populations correlated to the left and right hindbrain oscillators, respectively, and were thus anticorrelated to each other.

We next transitioned to single-neuron functional analysis, segmenting five neurons from each half of the hindbrain oscillator and three from each side of the inferior olive. **Figure 6c** shows the functional activity traces of these neurons, which were seen to fluctuate, similarly to the reference signal, on timescales of 20–30 s. As expected from the correlation coefficients, the left and right populations oscillated in antiphase, suggesting that these two populations may inhibit one another (**Fig. 6d**,**e**). Activity in the inferior olive was more weakly correlated to the reference signal (correlation coefficient ~ 0.2; **Fig. 6e**), and on the climbing phase of the fluctuations, it rose more slowly (**Fig. 6c**), consistent with a hypothesis under which inferior olive neurons are driven by the hindbrain oscillator.

The hindbrain-spinal circuit

In the same analysis, another reference signal was prominent across fish. This signal typically consisted of more punctate, temporally sparse activity. Because this signal is relatively regular on timescales of ~30 s, it was included in the selected low-frequency signals (**Fig. 5**, step 2). Following the same steps as above, we found that correlating the recorded volumes to this reference signal yielded an ordered population of neurons and neurite tracts that extended into the spinal cord (**Fig. 6f**,**g** and **Supplementary Video 8**). For brevity we refer to this as the hindbrain-spinal circuit. Segmentation of ten neurons from this population, and two areas of spinal cord neuropil, showed that single-neuron activity was highly correlated and that these neurons tended to be coactivated with activity in spinal cord neuropil (**Fig. 6h**).

Controls and consistency of results

The hindbrain oscillator and hindbrain-spinal circuit were consistently present across fish (**Supplementary Fig. 3** and **Supplementary Video 9**) and recovered in four out of five brains (Online Methods). To control for the possibility of human bias in selecting the reference signals (**Fig. 5**, step 3), we replaced the manual step by principal components analysis of the set of $\Delta F/F$ signals satisfying the long-timescale criterion (**Fig. 5**, step 2). Both the hindbrain oscillator and the hindbrain-spinal circuit were recovered (**Supplementary Fig. 4a** and Online Methods).

To test whether the neuronal populations identified above might arise from stimulation of the retina with blue laser light, we imaged only the hindbrain and spinal cord of a fish. The eyes, forebrain and midbrain were thus excluded from direct laser exposure, receiving only scattered light. Both the hindbrain oscillator and the hindbrain-spinal circuit were identified in this data set, which suggests that

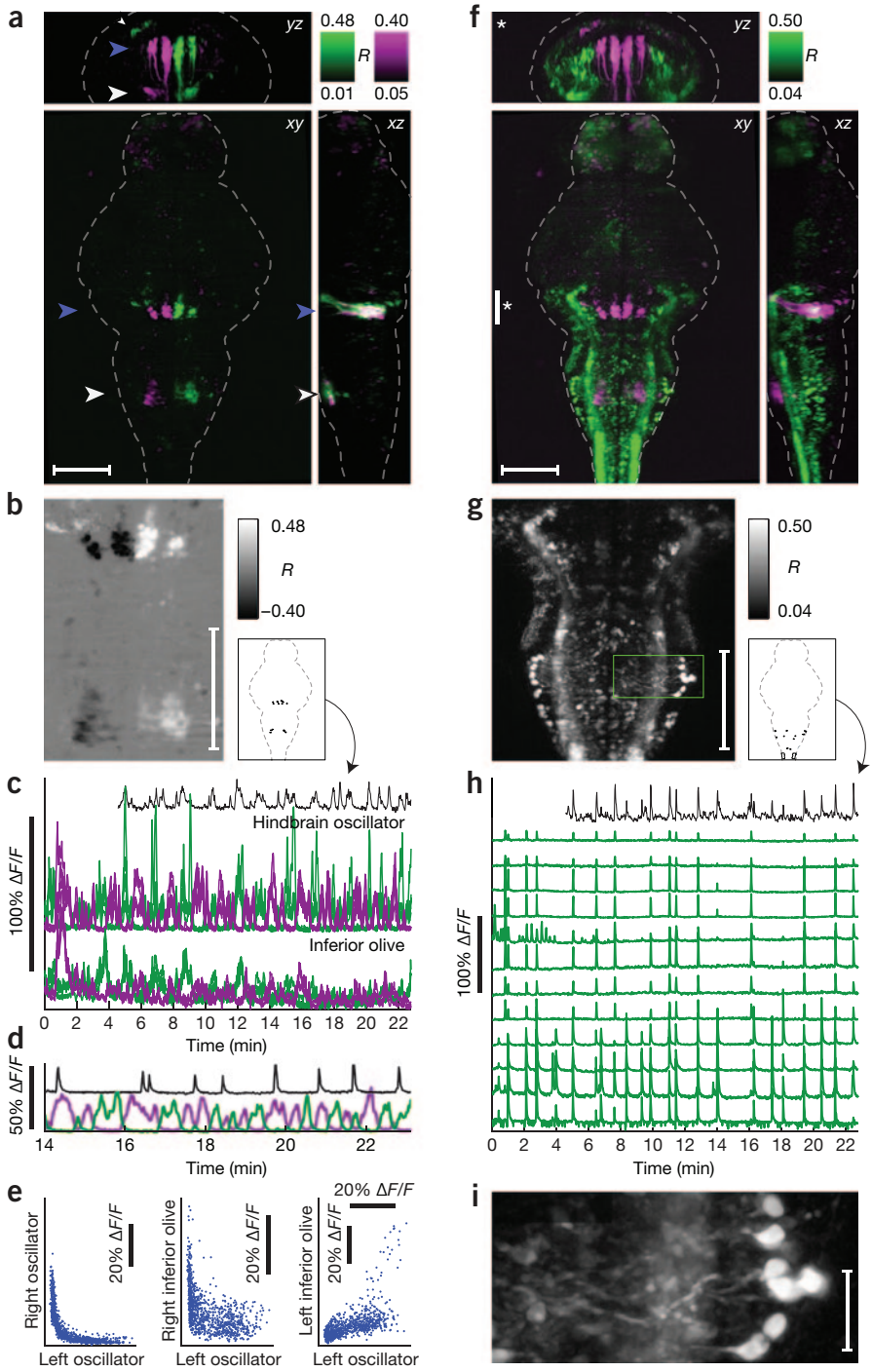

Figure 6 | Whole-brain, neuron-level identification of two functionally defined circuits. (**a**) Maximum-intensity projection of voxels positively (green) and negatively (magenta) correlated to the reference trace (black trace in **c**). Top, front projection. Bottom, top projection. Right, side projection. The hindbrain oscillator appears at single-neuron resolution in the anterior hindbrain (caudal to cerebellum; blue arrowheads). In addition, the inferior olive (white arrowheads) exhibits ipsilateral correlations to the hindbrain oscillator. (**b**) Enlarged view of hindbrain oscillator and inferior olive. (**c**) Functional GCaMP5G signals (as change in fluorescence, $\Delta F/F$) of ten manually isolated neurons in the hindbrain oscillator and six isolated neurons in the inferior olive, indicated in the map in **b**. Colors as in **a**. Reference signal is shown in black (first 4.5 min of data were discarded to avoid transient effects). (**d**) Average signal of all 16 neurons from **c**. For comparison, average signal from **h** is shown in black. The two signals are independent. (**e**) Scatter plots of left and right average population activity. (**f**) Spinal-hindbrain network, in the same fish, derived from the same time-lapse recording. Magenta, populations from **a**; green, correlation to a second functional trace (top trace in **h**). The *yz* projection (asterisk) is based on the volume section indicated by the white bar and asterisk in the *xy* projection. (**g**) Enlarged view of the spinal-hindbrain population. (**h**) Functional GCaMP5G signals in selected neurons of the spinal-hindbrain population and from two patches of neuropil in the spinal cord (top two traces). Reference signal is shown in black. (**i**) Detail of **g** showing neurites. Gamma was adjusted to aid visualization. Scale bars, 100 µm (**a**,**b**,**f**,**g**), 20 µm (**i**).

they are independent of direct retinal excitation (**Supplementary Fig. 4b**).

Finally, we confirmed that the neuronal populations were consistent across time. Anatomical maps derived separately for the first ~10 min and the last ~10 min of experimental time were almost identical (**Supplementary Fig. 5**).

DISCUSSION

It has been a long-standing goal in neuroscience to record activity from all neurons in the central nervous system of an organism. The system described here is capable of imaging, at the same time, single-neuron functional activity of more than 80% of the neurons in the brain of an intact, living vertebrate. Questions that were previously hampered by incomplete information about neuronal activity in the entire brain can now be addressed. Our identification of functionally defined networks represents a first step within the realm of possibilities opened up by functional whole-brain imaging.

The functions of the hindbrain oscillator and the hindbrain-spinal network in neural processing and behavior[26–28] remain to be elucidated. To our knowledge, the slow oscillations we observed in the inferior olive have not previously been reported, although in mammals, oscillations on the order of 3–5 s have been found in spiking patterns of single olivary neurons[29]. We conjecture that the hindbrain-spinal network is involved in locomotion, by virtue of the spinal cord activation and potential anatomical overlap with neuronal structures associated with swimming[22,23].

In the current experimental setup, the retina of the larval zebrafish is excited once per scanned volume, which limits the possibilities of visual stimulus delivery and may lead to activity induced by direct laser excitation of the retina. There are two pos-

sible solutions for future studies. The first is the use of two-photon excitation of the genetically encoded calcium indicator. The second is the use of multiple light sheets incident from at least two orthogonal directions. This latter approach would allow scanning of the majority of the brain with a laterally entering laser beam avoiding the eye and scanning of the remaining tissue in between the eyes with a separate laser beam entering from the anterior direction. Although some light-sensitive neurons exist outside the eyes of larval zebrafish, for example in the pineal gland, we do not expect these to strongly disrupt behavior and neural processing, in part because tectal responses have been found to be normal when measured with a confocal microscope[30], under which specimens are subjected to levels of light exposure substantially higher than those from a light-sheet microscope. The rate of volume acquisition, once per 1.3 s, allows us to capture many neuronal events, but higher speeds, allowing for more accurate resolution of spike timing, are of course desirable. Improvements in camera technology and complete elimination of timing overhead in the microscope control framework will enable a further increase of volumetric imaging speeds in the near future.

The larval zebrafish is gaining traction as a model system for systems neuroscience owing to advances in recording techniques and understanding of neuroanatomy and to an expanding knowledge of its behavioral repertoire. Motor[23,27], visual[30,31] and olfactory[32] systems have been successfully probed by electrophysiological and optical techniques, and sensorimotor processing and learning have been studied using functional imaging[9,33]. The current technique, possibly in combination with systems for monitoring behavior during brain scanning[9,21,28], holds promise for elucidating large-scale circuit function in each of these frontiers.

Combining our experimental approach to whole-brain functional imaging with sensory stimulation[27,32], behavioral readout[9,21], optogenetics[34] and analysis methods for high-dimensional data[3,7,35,36] will enable new system-level studies of the function of the vertebrate nervous system.

METHODS

Methods and any associated references are available in the online version of the paper.

Note: Supplementary information is available in the online version of the paper.

ACKNOWLEDGMENTS

We thank M. Coleman (Coleman Technologies) for custom microscope operating software; D. Robson, J. Li, A. Schier and F. Engert (Harvard) for sharing the transgenic *elavl3:GCaMP5G* fish; C. Riegler (Harvard) for providing this line in the *albino* background; Janelia Farm Research Campus Instrument Design and Fabrication for custom mechanical parts; Janelia Farm Research Campus Vivarium staff for animal care; M. Orger, R. Tomer, L. Lagnado and L. Looger for their contributions to early GCaMP test experiments using light-sheet microscopy; K. Branson, V. Jayaraman, L. Looger, K. Svoboda, F. Amat, W. Lemon and M. Yartsev for helpful discussions and critical reading of the manuscript; and A. Kampff and F. Engert (Harvard) for sharing the two-photon volumetric imaging data. This work was supported by the Howard Hughes Medical Institute.

AUTHOR CONTRIBUTIONS

M.B.A. and P.J.K. conceived of the research, performed the experiments, analyzed the data and wrote the paper.

COMPETING FINANCIAL INTERESTS

The authors declare no competing financial interests.

1. Averbeck, B.B., Latham, P.E. & Pouget, A. Neural correlations, population coding and computation. *Nat. Rev. Neurosci.* **7**, 358–366 (2006).
2. Friedrich, R.W., Habermann, C.J. & Laurent, G. Multiplexing using synchrony in the zebrafish olfactory bulb. *Nat. Neurosci.* **7**, 862–871 (2004).
3. Schneidman, E., Berry, M.J. II, Segev, R. & Bialek, W. Weak pairwise correlations imply strongly correlated network states in a neural population. *Nature* **440**, 1007–1012 (2006).
4. Stopfer, M., Jayaraman, V. & Laurent, G. Intensity versus identity coding in an olfactory system. *Neuron* **39**, 991–1004 (2003).
5. Druckmann, S. & Chklovskii, D.B. Neuronal circuits underlying persistent representations despite time varying activity. *Curr. Biol.* **22**, 2095–2103 (2012).
6. Gregoriou, G.G., Gotts, S.J. & Desimone, R. Cell-type-specific synchronization of neural activity in FEF with V4 during attention. *Neuron* **73**, 581–594 (2012).
7. Churchland, M.M. *et al.* Neural population dynamics during reaching. *Nature* **487**, 51–56 (2012).
8. Deco, G., Jirsa, V.K. & McIntosh, A.R. Emerging concepts for the dynamical organization of resting-state activity in the brain. *Nat. Rev. Neurosci.* **12**, 43–56 (2011).
9. Ahrens, M.B. *et al.* Brain-wide neuronal dynamics during motor adaptation in zebrafish. *Nature* **485**, 471–477 (2012).
10. Flusberg, B.A. *et al.* High-speed, miniaturized fluorescence microscopy in freely moving mice. *Nat. Methods* **5**, 935–938 (2008).
11. Katona, G. *et al.* Fast two-photon *in vivo* imaging with three-dimensional random-access scanning in large tissue volumes. *Nat. Methods* **9**, 201–208 (2012).
12. Holekamp, T.F., Turaga, D. & Holy, T.E. Fast three-dimensional fluorescence imaging of activity in neural populations by objective-coupled planar illumination microscopy. *Neuron* **57**, 661–672 (2008).
13. Grewe, B.F., Langer, D., Kasper, H., Kampa, B.M. & Helmchen, F. High-speed *in vivo* calcium imaging reveals neuronal network activity with near-millisecond precision. *Nat. Methods* **7**, 399–405 (2010).
14. Cheng, A., Goncalves, J.T., Golshani, P., Arisaka, K. & Portera-Cailliau, C. Simultaneous two-photon calcium imaging at different depths with spatiotemporal multiplexing. *Nat. Methods* **8**, 139–142 (2011).
15. Marre, O. *et al.* Mapping a complete neural population in the retina. *J. Neurosci.* **32**, 14859–14873 (2012).
16. Akerboom, J. *et al.* Optimization of a GCaMP calcium indicator for neural activity imaging. *J. Neurosci.* **32**, 13819–13840 (2012).
17. Park, H.C. *et al.* Analysis of upstream elements in the *Hu*C promoter leads to the establishment of transgenic zebrafish with fluorescent neurons. *Dev. Biol.* **227**, 279–293 (2000).
18. Naumann, E.A., Kampff, A.R., Prober, D.A., Schier, A.F. & Engert, F. Monitoring neural activity with bioluminescence during natural behavior. *Nat. Neurosci.* **13**, 513–520 (2010).
19. Tomer, R., Khairy, K., Amat, F. & Keller, P.J. Quantitative high-speed imaging of entire developing embryos with simultaneous multiview light-sheet microscopy. *Nat. Methods* **9**, 755–763 (2012).
20. Keller, P.J., Schmidt, A.D., Wittbrodt, J. & Stelzer, E.H.K. Reconstruction of zebrafish early embryonic development by scanned light sheet microscopy. *Science* **322**, 1065–1069 (2008).
21. Sumbre, G., Muto, A., Baier, H. & Poo, M.M. Entrained rhythmic activities of neuronal ensembles as perceptual memory of time interval. *Nature* **456**, 102–106 (2008).
22. Kinkhabwala, A. *et al.* A structural and functional ground plan for neurons in the hindbrain of zebrafish. *Proc. Natl. Acad. Sci. USA* **108**, 1164–1169 (2011).
23. Koyama, M., Kinkhabwala, A., Satou, C., Higashijima, S. & Fetcho, J. Mapping a sensory-motor network onto a structural and functional ground plan in the hindbrain. *Proc. Natl. Acad. Sci. USA* **108**, 1170–1175 (2011).
24. Leopold, D.A., Murayama, Y. & Logothetis, N.K. Very slow activity fluctuations in monkey visual cortex: implications for functional brain imaging. *Cereb. Cortex* **13**, 422–433 (2003).
25. Junek, S., Chen, T.W., Alevra, M. & Schild, D. Activity correlation imaging: visualizing function and structure of neuronal populations. *Biophys. J.* **96**, 3801–3809 (2009).
26. Hatta, K. & Korn, H. Tonic inhibition alternates in paired neurons that set direction of fish escape reaction. *Proc. Natl. Acad. Sci. USA* **96**, 12090–12095 (1999).

27. Orger, M.B., Kampff, A.R., Severi, K.E., Bollmann, J.H. & Engert, F. Control of visually guided behavior by distinct populations of spinal projection neurons. *Nat. Neurosci.* **11**, 327–333 (2008).
28. Miri, A. *et al.* Spatial gradients and multidimensional dynamics in a neural integrator circuit. *Nat. Neurosci.* **14**, 1150–1159 (2011).
29. Chorev, E., Yarom, Y. & Lampl, I. Rhythmic episodes of subthreshold membrane potential oscillations in the rat inferior olive nuclei *in vivo*. *J. Neurosci.* **27**, 5043–5052 (2007).
30. Nikolaou, N. *et al.* Parametric functional maps of visual inputs to the tectum. *Neuron* **76**, 317–324 (2012).
31. Del Bene, F. *et al.* Filtering of visual information in the tectum by an identified neural circuit. *Science* **330**, 669–673 (2010).
32. Blumhagen, F. *et al.* Neuronal filtering of multiplexed odour representations. *Nature* **479**, 493–498 (2011).
33. Aizenberg, M. & Schuman, E.M. Cerebellar-dependent learning in larval zebrafish. *J. Neurosci.* **31**, 8708–8712 (2011).
34. Douglass, A.D., Kraves, S., Deisseroth, K., Schier, A.F. & Engert, F. Escape behavior elicited by single, channelrhodopsin-2-evoked spikes in zebrafish somatosensory neurons. *Curr. Biol.* **18**, 1133–1137 (2008).
35. Paninski, L. *et al.* A new look at state-space models for neural data. *J. Comput. Neurosci.* **29**, 107–126 (2010).
36. Yu, B.M. *et al.* Gaussian-process factor analysis for low-dimensional single-trial analysis of neural population activity. *J. Neurophysiol.* **102**, 614–635 (2009).

ONLINE METHODS

Fast volumetric light sheet–based imaging. The improvement in sustained volumetric imaging speed, i.e., the sustained number of volume elements recorded per time unit, is the result of four conceptual extensions of the hardware and software of the previously developed SiMView light-sheet microscopy platform[19].

First, volumetric imaging is performed by laser scanning in two directions and movement of the detection objective, thus eliminating the need for sample movement. The light sheet is created and displaced by a fast piezo-operated two-axis tip/tilt mirror (S-334, Physik Instrumente). The orientations of the mirror axes are converted into x and z axes in sample space by using coupled voltage input signals. The two main motions, planar illumination by fast scanning along the x axis and light-sheet displacement by slow scanning along the z axis, are realized by combining precalculated voltage ramps from two independent I/O boards (PXI-6733, National Instruments). Four ramps are needed per tip/tilt mirror, corresponding to the virtual x and z components of each of the two physical tip/tilt mirror axes. These simple linear voltage ramps are combined with fast summing amplifiers (SIM980 in SIM900 mainframe, Stanford Research Systems) to create final voltage vectors for each of the two physical tip/tilt axes over the course of one volumetric scan. This approach allows us to eliminate the communication bottlenecks in the execution of a conventional SiMView volumetric imaging experiment because it avoids constraints imposed by the limited buffer size and typical time overhead of several milliseconds involved in resetting the buffer of the I/O electronics controlling the microscope.

Second, the displacement of the focal plane with a piezo-operated detection objective[12,20] (P-622.1CD PIHera piezo stage, Physik Instrumente) greatly reduces the settle time for each plane acquisition step (as compared to that of sample displacement with a linear motor), thereby avoiding a performance bottleneck arising from the use of a discrete stepping mode, and allows us to optimize the spatial offset of the focal plane as a function of imaging depth in the specimen, thus improving overall image quality.

Third, we combined the optoelectronics approach to high-speed volumetric imaging with a fast computational pipeline that enables high-speed image acquisition continuously for up to several days.

Fourth, we replaced the first-generation sCMOS cameras and CameraLink frame grabbers of the SiMView microscope with faster hardware (Orca Flash 4.0, Hamamatsu). The resulting improvement in raw image acquisition rate ensures that the complementary performance improvements introduced above are not constrained by possible overhead in the detection system of the microscope. In the current implementation of the acquisition workflow, camera performance is approximately on par with the performance of the microscope control framework.

We used the new high-speed imaging mode to record volumes of $800 \times 600 \times 200\ \mu m^3$ with 41 image planes in 1.3 s (5-µm step size between adjacent planes), using an optical configuration providing a 4.25 ± 0.80–µm–thick light sheet (full width at half maximum, mean ± s.d. across the brain volume, $n = 81$) and an effective lateral resolution of 0.65 µm (ref. 19).

The geometry of the illuminating laser beam can be approximated by Gaussian beam optics, and we measured a central thickness of 3.25 µm and a maximum thickness of 6.50 µm at the edge of the field of view. Note that this light-sheet geometry deviates from the commonly used Rayleigh criterion (for which light-sheet thickness at the edge of the field of view is $\sqrt{2}\times$ larger than the central thickness) and was chosen to minimize the average light-sheet thickness across the actual volume occupied by the zebrafish larval brain. We determined the thickness of the light-sheet profile as a function of location in the field of view by deflecting the scanned light sheet onto the camera using a mirror in the specimen chamber and imaging a cross-section of the profile every 10 µm along the illumination axis. A three-dimensional map representing the entire imaging volume was constructed from these measurement points and segmented using the outline of the zebrafish larval brain obtained from the functional imaging experiments. The data points within the brain volume were then used to calculate the mean and s.d. of light-sheet thickness across the brain volume.

The imaging strategy outlined above allowed us to obtain whole-brain GCaMP5G recordings at a rate of 0.8 Hz, yielding an average data set size of 1 TB (corresponding to 1 h of continuous volumetric high-speed imaging) per recorded specimen. Despite the sustained high-speed image acquisition, photobleaching rates over the course of these experiments were negligible. Because slight variations in orientation of the fish larvae can occur during sample preparation, we addressed tilts of the body axis with respect to the image plane by imaging a correspondingly larger sample volume. In some experiments (**Fig. 2**), volumetric imaging was therefore performed at a slightly longer time interval of 1.4 s. The expected performance with respect to spatial resolution and temporal sampling in two additional imaging scenarios (volumes smaller or larger than the zebrafish brain) is discussed in **Supplementary Note 1**.

In all experiments, a power of 0.3 mW was used for illumination with laser light at 488 nm, leading to 1.5-µJ laser light exposure in each brain slice per volumetric scan. By measuring the average intensity level of randomly selected cell bodies (I) and the s.d. of intensity levels in background regions (σ), we determined the signal-to-noise ratio in these recordings to be $I/\sigma = 180 \pm 11$ (mean ± s.e.m., $n = 31$). Fluorescence light was collected with Plan-Apochromat 20×/1.0 W (Carl Zeiss) or CFI75 LWD 16×/0.80 W (Nikon) objectives and filtered with a BrightLine BP525/50 band pass (Semrock). A comprehensive list of all hardware components of the microscope, the image acquisition pipeline and the data storage framework is provided in **Supplementary Table 1**.

Animal husbandry. All experiments were conducted according to protocols approved by the Institutional Animal Care and Use Committee of the Howard Hughes Medical Institute, Janelia Farm Research Campus.

Zebrafish sample preparation. For acute imaging in the light-sheet microscope, 5-d-old zebrafish larvae of the *elavl3:GCaMP5G* line in *albino* background were embedded in 1.5% low-melting-temperature agarose (SeaPlaque, Lonza; prepared in filtered fish facility water) inside a glass capillary (1.5/2.0-mm inner/outer diameter, 20-mm length; Hilgenberg GmbH). The larvae were centered in the capillary and oriented using cut-off Microloader pipette tips (Eppendorf). After gel formation, we extruded the section of the agarose cylinder containing the head of the larva from the capillary by inserting wax into the capillary on the side opposite to the fish. The sample chamber of the light-sheet microscope was filled with filtered fish facility water, and the capillary was inserted for imaging. Specimens were maintained at room temperature throughout the imaging period. After the

experiment, specimens were kept in a Petri dish for several days to control for normal development.

Comparative neuron segmentation. Complementing our analysis of image contrast and lateral resolution in the functional light-sheet microscopy data (**Supplementary Fig. 1**), we performed a second analysis to validate that (i) neighboring neurons are generally separable along the detection axis (i.e., when separation based solely on lateral features is not possible) and (ii) almost all cell bodies within the scanned volume are detected. To this end, we manually segmented cell bodies in midbrain and hindbrain regions in light-sheet microscopy recordings as well as point-scanning two-photon microscopy reference recordings and compared the densities of detected cells. In the two-photon reference recording, using an Olympus 20×/0.95 objective and a voxel size of $0.2 \times 0.2 \times 1.0\ \mu m^3$, the anatomy of cell bodies was highly oversampled, which makes the measured cell densities well suited for defining a gold-standard reference.

To arrive at a conservative estimate of the physical coverage of neurons in the functional light-sheet recordings, we first measured cell densities in multiple brains of comparable age to determine the deviation of this parameter. We then compared, in the worst-case scenario, measured cell densities in the functional light-sheet recording to that obtained from the gold-standard two-photon data set.

In the first step, we performed cell density measurements in the midbrain as well as in the hindbrain of three brains of similar age, using our functional light-sheet recordings. This analysis showed that measured cell densities deviate across brains by 0.92% in the midbrain (s.d., $n = 1{,}076$) and by 1.19% in the hindbrain (s.d., $n = 1{,}366$). From this, we conclude that cell densities (at least in these two brain areas) are relatively robust across specimens of comparable age.

We controlled for double-counting in the functional light-sheet recordings by automatically discarding centroids in close lateral proximity for neighboring planes (lateral distance of 1.2 µm or less). To quantify the effectiveness of this correction step, we performed a side-by-side comparison using the first stack of a functional light-sheet recording (with 5-µm z-step size) as well as a high-resolution light-sheet reference stack recorded from the same brain just a few seconds before the onset of functional imaging (with 1-µm z-step size). This analysis provided a correspondence of cell counts of 97.4% ($n = 535$).

Finally, we compared cell densities in the functional light-sheet recordings and in the two-photon gold-standard reference recording (of a different brain of comparable age). To arrive at the most conservative estimate, we assumed a worst-case scenario from the perspective of the light-sheet recordings: instead of averaging over cell densities in all three light-sheet recordings, we used only the cell densities for the brain for which we measured the maximum deviation in cell densities from that of the two-photon recording, thus explicitly taking into account the possibility of biological differences in cell densities in different brains. We obtained cell densities of $6.99 \pm 0.26 \times 10^{-3}\ \mu m^3$ and $6.00 \pm 0.28 \times 10^{-3}\ \mu m^3$ in midbrain and hindbrain regions of the two-photon reference recording ($n = 179$ and 119). From the light sheet–based measurement exhibiting the largest deviation from the two-photon results, we obtained cell densities of $6.44 \pm 0.17 \times 10^{-3}\ \mu m^3$ and $5.81 \pm 0.14 \times 10^{-3}\ \mu m^3$ in midbrain and hindbrain regions ($n = 354$ and 451). The average fraction of measured cell densities is thus 94.5%. Subsequently, we further reduced this fraction by multiplication with the fraction of cell counts obtained in the light-sheet side-by-side comparison (97.4%), thus explicitly taking into account the statistics for double-counting in the analysis of the functional light-sheet recordings.

Thus, we estimate that for regions captured with subcellular lateral resolution, the functional light-sheet data sets revealed on average 92.0% of all neurons with single-cell resolution.

Image processing. Functional signals were extracted from the volumetric time series via the usual $\Delta F/F$ measure, using a sliding window analysis for determining reference intensity levels corresponding to zero activity. A reference anatomical volume $REF_{x,y,z}$ was defined as the average of ten subsequent imaged volumes in the middle of the experiment. Then a custom nonlinear image registration algorithm was applied to all recorded planes to align each plane to the corresponding plane in the reference volume and to correct for any tissue deformations resulting from movement of the fish, drift of the sample or subtle developmental changes. First, a rigid translation in x and y—based on standard 2D convolution techniques—was applied to roughly align a plane to its corresponding reference plane. Second, points $p_{x,y}$ were chosen every 30 µm in x and y. Centered at every point, a square of $50 \times 50\ \mu m^2$ was aligned to the reference plane using the same type of rigid transformation, which generated displacement vectors d_x and d_y at every point $p_{x,y}$. Finally, every voxel was displaced by the maximum of d_x and d_y in a $50 \times 50\ \mu m^2$ neighborhood around the voxel. This scheme is capable of correcting for local warping of the tissue in the x and y directions. See **Supplementary Note 2** for a quantification of typical tissue movements. Although the mapping is not always continuous, we found that the displacements were small enough to yield accurate registration in almost all cases. After registration of all planes, functional signals at time t and voxel (x, y, z) were defined as $(\Delta F(t)/F)_{x,y,z} = (F(t)_{x,y,z} - REF_{x,y,z})/REF_{x,y,z}$.

In the specific case of the brain-area analysis of **Figure 3**, note that local and projection fibers may add to the average signal and that the average signal may weigh certain neurons more strongly owing to tissue inhomogeneities and their effect on signal detection efficiency.

The code modules for image registration and $\Delta F/F$ calculation were written in Matlab (MathWorks). This code is provided as **Supplementary Software** and described in the supplementary information.

Evaluation of activity in habenula neurons correlated to hindbrain activity. In **Figure 4**, we investigated the functional coupling between activity of habenula neurons and average hindbrain activity. The correlation coefficient between hindbrain activity and the average activity of the 100 most correlated neurons is 0.52, and that of the 100 most anticorrelated neurons is –0.42. To verify that these values are not artifacts of the ordering of the habenula signals, we applied a shuffle test, swapping the first and second halves of the time series of the habenula neurons. If our observations arose from chance, this operation would be expected to not sizably change the correlation coefficients. Instead, it led to a decrease in correlation coefficients to 0.12 and –0.11, showing that single-neuron correlations to hindbrain activity are indeed present. Individual neuron correlations ranged between –0.57 and 0.51; scrambled, between

doi:10.1038.nmeth.2434

–0.10 and 0.08; the number of neurons with a small correlation coefficient, between –0.1 and 0.1, was 99; the number of neurons greater than 0.1 or less than –0.1 was 204.

Semiautomated analysis for the extraction of functionally defined neural circuits. The goal of this analysis is the identification of large neuronal populations across the brain with collective activity on long timescales.

First, the scanned volume was divided into supervoxels (**Fig. 5**, step 1), each approximately the size of a neuron ($5 \times 5 \times 5\ \mu m^3$).

Second, the power spectra of the corresponding $\Delta F/F$ time series were computed using the fast Fourier transform (over 22 min of experimental time, with the first 4.5 min of data discarded to avoid transient effects). This reduction to supervoxels not only introduces a practical length scale but also allows for a 200-fold speed-up of the automated part of the analysis. Only supervoxels with slowly varying activity were selected. The power spectrum of the $\Delta F/F$ time series was used to select for traces containing long timescales: the 2,000 traces with the largest difference between power in the slow (10–30 s) and fast (2–10 s) power bands were used for further analysis (**Fig. 5**, step 2).

Third, supervoxels were ordered according to the total number of other supervoxels with highly correlated $\Delta F/F$ signals, biasing subsequent analysis to large, correlated neuronal populations. This is shown as a correlation matrix in **Figure 5** (step 3), where the supervoxels are ordered such that the rightmost column contains the largest number of entries greater than 0.5, and the leftmost column contains the smallest number of such entries. Columns further to the right are more likely to correspond to large populations of correlated neurons. In this representation, clusters become apparent in the form of blocks around the diagonal; each cluster represents an anatomical pattern of correlated supervoxels, which is a candidate for a functional circuit. Of course, detection of correlated activity is subject to the usual caveats of calcium imaging[16]: for example, single spikes may go undetected, and neurons with high firing rates may have a higher chance of being included in the correlation analysis.

Fourth, a manual step followed, in which several reference fluorescence traces were determined by selecting supervoxels from each cluster in the ordered correlation matrix (**Fig. 5**, step 4). The supervoxels with high correlation, or anticorrelation, to the reference signals were visualized (**Fig. 5**, step 5) and often exhibited ordered anatomical structure suggestive of neuronal circuits.

At this point, importantly, the method transitioned from supervoxel-based analysis to voxel-based anatomical analysis with subcellular resolution. The supervoxelization of the volume was discarded, and only the reference traces were used for further analysis. The correlation coefficients between the intensity of every voxel in the volumetric time series and the reference trace were computed to generate a brain-sized volume of correlation coefficients (**Fig. 5**, step 6).

A priori, there is no guarantee that the volume of correlation coefficients has any anatomical structure, given that it is not based on an anatomical segmentation of the tissue. However, owing to the fact that voxel values within neurons co-vary and that, evidently, activity can co-vary across neurons, the volume of correlation coefficients showed clear single-neuron shapes, neurite tracts and population-scale structure that appeared structurally ordered and were reproducible across multiple brains, both by anatomical appearance and in terms of the general structure of their $\Delta F/F$ signals (**Fig. 6** and **Supplementary Fig. 3**). The anatomical structure was largely insensitive to the identity of the voxel selected within a given cluster in step 4. The voxel-based correlation coefficients between voxels in these structures and the reference signal were high, often on the order of 0.2–0.6 (the correlation coefficients between single-neuron activity and the reference trace are likely to be even higher, as voxel-by-voxel recording noise will even out when averaging over the voxels constituting a neuron). These observations strongly suggest that the retrieved structures are functionally related neuronal populations, which becomes even more evident when looking at the activity of sets of segmented single neurons from these populations.

Finally, single neurons were manually segmented from the volume of correlation coefficients, and their $\Delta F/F$ time series were extracted as the average of the $\Delta F/F$ values of the voxels within the segmented neuron (for example, **Fig. 6c**).

The code modules for data analysis and data visualization were written in Matlab. This code is provided as **Supplementary Software** and described in the supplementary information.

Consistency across fish, and controlling for eye stimulation and human selection bias. Supplementary Figure 3 shows data from two additional fish, in which both the hindbrain oscillator (**Supplementary Video 9**) and the hindbrain-spinal circuit were identified (the hindbrain-spinal circuit of **Supplementary Fig. 3e** is shown in **Supplementary Fig. 4b**). Both circuits were consistently present across fish and recovered in four out of five brains. To control for the possibility of human bias in selecting the reference signals (**Fig. 5**, step 3), we replaced the manual step by principal components analysis (PCA) on the set of $\Delta F/F$ signals satisfying the long-timescale criterion (**Fig. 5**, step 2; same ~20 min of data used). Specifically, if the $\Delta F/F$ signals are represented by matrix containing the fluorescence traces of supervoxels as rows, with supervoxels arranged in columns, the principal components (PCs) were recovered in Matlab using the operation coeff = pca($\Delta F/F$), where the first n columns of "coeff" represent the first n PCs. When we set the reference signals to be the first two PCs, both the hindbrain oscillator and the hindbrain-spinal circuit were recovered (**Supplementary Fig. 4a**), but the populations were mixed. For instance, the second PC generated a mixture of the oscillator and the hindbrain-spinal circuit; the first PC generated a mixture of these two and weak correlations in the forebrain. Looking beyond the first two PCs yielded similar results (for completeness, eigenvalues for the first six PCs were 0.098, 0.071, 0.050, 0.036, 0.027 and 0.023). There are two implications. First, PCA does not offer an improvement over the manual step in the analysis for this data set. Second, the fact that the populations extracted using the PCA step are similar to those extracted using the manual step rules out the possibility that the hindbrain oscillator and the hindbrain-spinal network are artifacts of human selection bias in the semiautomated analysis.

In this study, we used light-sheet illumination from the side and, to maximize physical coverage of the brain, did not avoid the eye. Neural activity in these conditions may represent naturally occurring spontaneous activity or activity that depends on the experimental conditions, including the presence of blue excitation light. Periodic activity locked to the excitation of the retina may introduce an offset in fluorescence measurements, whereas

long-term effects may include, for example, changes in the excitability of a neural circuit. To test whether the neuronal populations identified above might arise from stimulation of the retina with blue laser light, we imaged only the hindbrain and spinal cord of a fish, with its eyes, forebrain and midbrain excluded from direct laser exposure. Both the hindbrain oscillator and the hindbrain-spinal circuit were identified in this data set, showing that they are independent of retinal excitation (**Supplementary Fig. 4b**).

Of course, it is unknown whether the two circuits consist of the same set of genetically defined neurons across fish: the names assigned to them are only based on their temporal patterns of activity and their general anatomical features. Within fish, however, the neuronal populations were consistent across time, so that the anatomical maps derived separately for the first ~10 min and the last ~10 min of experimental time were almost identical (**Supplementary Fig. 5**).

It is remarkable—and, for us, unexpected—that structures such as the hindbrain oscillator, which appears anatomically structured and, combined with the inferior olive, is localized to only six clusters of cells in the entire brain, can be recovered by simply correlating all ~10^8 voxels of the volumetric $\Delta F/F$ signals, over less than 20 min of data, to a single reference signal without further statistical processing. Because our analysis method is computationally straightforward, we interpret this as a testimony to the power of whole-brain functional imaging.

doi:10.1038.nmeth.2434